First-Year and Multiyear Sea Ice Incidence Angle Normalization of Dual-Polarized Sentinel-1 SAR Images in the Beaufort Sea

Wiebke Aldenhoff, Leif E. B. Eriksson, Yufang Ye, and Céline Heuzé

***Abstract*—Automatic and visual sea ice classification of SAR imagery is impeded by the incidence angle dependence of backscatter intensities. Knowledge of the angular dependence of different ice types is therefore necessary to account for this effect. While consistent estimates exist for HH polarization for different ice types, they are lacking HV polarization data, especially for multiyear sea ice. Here we investigate the incidence angle dependence of smooth and rough/deformed first-year and multiyear ice of different ages for wintertime dual-polarization Sentinel-1 C-band SAR imagery in the Beaufort Sea. Assuming a linear relationship, this dependence is determined using the difference in incidence angle and backscatter intensities from ascending and descending images of the same area. At cross-polarization rough/deformed first-year sea ice shows the strongest angular dependence with -0.11 dB/1° followed by multiyear sea ice with -0.07 dB/1°, and old multiyear ice (older than three years) with -0.04 dB/1°. The noise floor is found to have a strong impact on smooth first-year ice and estimated slopes are therefore not fully reliable. At co-polarization, we obtained slope values of -0.24, -0.20, -0.15, and -0.10 dB/1° for smooth first-year, rough/deformed first-year, multiyear, and old multiyear sea ice, respectively. Furthermore, we show that imperfect noise correction of the first subswath influences the obtained slopes for multiyear sea ice. We demonstrate that incidence angle normalization should not only be applied to co-polarization but should also be considered for cross-polarization images to minimize intra ice type variation in backscatter intensity throughout the entire image swath.**

***Index Terms*—Incidence angle, sea ice, Sentinel-1.**

I. Introduction

DUAL-POLARIZATION synthetic aperture radar (SAR) imagery has become a standard for recent Earth observation satellite SAR systems, and the Copernicus Sentinel-1 mission made such data easily accessible for research. The cross-polarization channel contains complementary information to the co-polarization channel for sea ice applications. It supports, for example, the discrimination of first-year sea ice (FYI) and multiyear sea ice (MYI) and the identification of deformation features like ridges; see, e.g., [1] and [2]. Moreover, the incidence angle dependence of radar backscatter is expected to be lower at cross-polarization compared to co-polarization, reducing backscatter variations over the image swath and enhancing the ice–water contrast [3].

Recent studies of satellite C-band SAR imagery, however, indicate that the incidence angle dependence of FYI is in a range where incidence angle normalization could be beneficial for automatic and visual image interpretation and classification. Reported incidence angle slopes at cross-polarization vary from insignificant for all ice types to -0.25, -0.16, -0.13, and -0.07 dB/1° for level land fast, deformed, general first-year, and MYI, respectively [4]–[7]. Typical slope values at HH co-polarization vary between -0.27 and -0.16 dB/1° for level FYI and MYI, respectively [6], [8]. Incidence angle normalization is regularly applied at co-polarization for various image classification tasks, e.g., [9]–[12]. Comparison of the above values for incidence angle dependence at co- and cross-polarization indicates that incidence angle correction should be considered at cross-polarization particularly for FYI.

Incidence angle dependence of MYI at cross-polarization has been estimated from SAR images by a few studies only and their results vary from insignificant to -0.07 dB/1° [4], [7]. Though much lower, there is a need to better quantify the incidence angle dependence of MYI at cross-polarization and to assess the impact of incidence angle induced backscatter variations for MYI. This is of particular interest for wide swath imageries that usually cover a wide range of incidence angles from about 20° to 50° and are used for operational ice charting.

A linear relationship between incidence angle and radar backscatter in dB can be assumed as a first-order approximation of the true relationship in the incidence angle range between 20° and 50° [13]. In the literature, two different approaches have been used to determine the incidence angle dependence. On the one hand, direct slope estimation from backscatter intensity versus incidence angle plots. On the other hand, slope estimates from plots of the difference in backscatter intensity versus difference in incidence angle of the same patch of sea ice observed from two different angles, i.e., ascending and descending images obtained within short time frames. The former has strength in its

Manuscript received September 2, 2019; revised December 30, 2019 and February 2, 2020; accepted February 14, 2020. Date of publication April 3, 2020; date of current version April 28, 2020. This work was supported by the Swedish National Space Agency (Dnr. 164/18 and Dnr. 192/15). *(Corresponding author: Wiebke Aldenhoff.)*

Wiebke Aldenhoff and Leif E. B. Eriksson are with the Department of Space, Earth and Environment, Chalmers University of Technology, 41296, Gothenburg, Sweden (e-mail: wiebke.aldenhoff@chalmers.se; leif.eriksson@chalmers.se).

Yufang Ye is with the Southern Marine Science and Engineering Guangdong Laboratory (Zhuhai), Zhuhai, 519082, PR China and School of Geospatial Engineering and Science, Sun Yat-Sen University, Guangzhou 519082, PR China (e-mail: yeyf8@mail.sysu.edu.cn).

Céline Heuzé is with the Department of Earth Sciences, University of Gothenburg, 40530, Gothenburg, Sweden (e-mail: celine.heuze@gu.se).

Digital Object Identifier 10.1109/JSTARS.2020.2977506

simplicity and it can be directly estimated from the scene in use. The latter is more robust against intra ice type variability but requires more than one image to determine the parameters [14]. In this study, the difference in incidence angle and backscatter intensity between ascending and descending imagery is used to determine the incidence angle dependence.

Sentinel-1 A/B has become one of the main sources for C-band SAR imagery of sea ice due to its operational and therefore predictable acquisitions [15] as well as the open data policy of the Copernicus program. Changes in observation strategy made ascending/descending dual-polarization data over large areas of the Arctic only available until April 2017. Moreover, the cross-polarization channel of Sentinel-1 images has been affected by azimuth scalloping noise and an incidence angle dependent noise floor [16]. A new noise correction strategy has therefore been introduced for images acquired after March 2018 to mitigate these problems.

In this study, we investigate the incidence angle dependence of wintertime FYI and MYI for dual-polarization Sentinel-1 C-band SAR images with emphasis on the cross-polarization channel. We limit this work to wintertime imagery because separation of ice types becomes challenging under melt conditions at C-band [17] and is therefore left for future studies. The availability of suitable dual-polarization ascending and descending imagery, e.g., the occurrence of FYI and MYI, restricted the study area and time period to the Eastern Beaufort Sea during the winter 2016/2017. We used, however, imagery of the same area from the winter 2018/2019 to evaluate the impact of the improved noise correction by comparison of direct slope estimates from FYI. With this study, we aim to bridge the gap regarding quantification of the incidence angle dependence of MYI at cross-polarization from SAR data. Furthermore, we investigate the effect of incidence angle normalization on overlays of SAR images with a large difference in incidence angle.

II. Study Area and Data

A. Study Area

The study area is located in the eastern part of the Beaufort Sea, in the Arctic (Fig. 1). FYI is dominant in the southern part, while MYI is found in the northern part of the study area. The occurrence of FYI and MYI is typical for this area where sea ice motion is dominated by the anticyclonic Beaufort Gyre that transports MYI from the central Arctic to this area [18], [19]. The main study period covers wintertime from December 2016 to early March 2017, therefore limiting the effects of diurnal variations in radar backscatter. The maximum daily air temperatures from ERA5 throughout the observation period are shown in Fig. 2 [20]. ERA5 is the most recent atmospheric reanalysis dataset from the European Centre for Medium-Range Weather Forecasts and is available through the Copernicus Climate Change Service. They are consistently negative, and, hence, we can confirm cold winter conditions. Sea ice drift, estimated from position differences of the samples from the used image pairs, varied from almost insignificant at areas close to land to 16 cm/s with an average of 7 and 10 cm/s for FYI and MYI, respectively. These values are within the range of sea ice velocities expected for this area [21], [22].

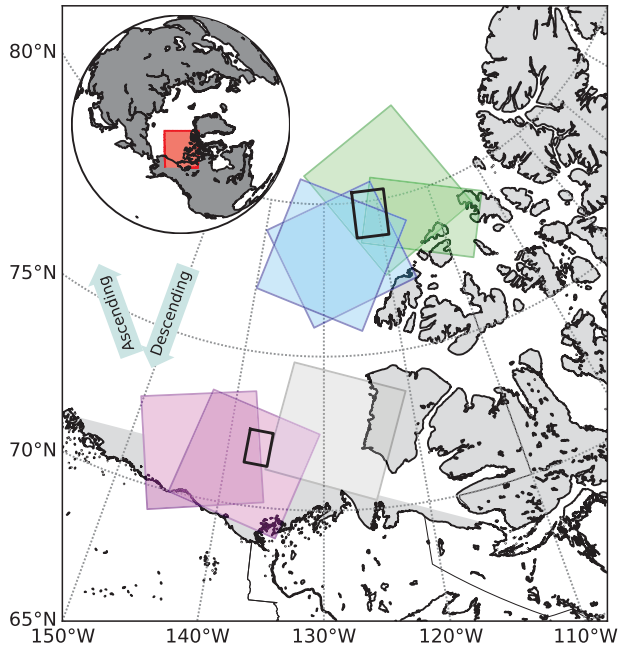

Fig. 1. Map of the study area where violet, blue, and green areas outline images used to study first-year, multiyear, and old multiyear sea ice, respectively. Grey area outlines images from 2019. Black rectangles mark areas of mosaics presented in Section IV-C.

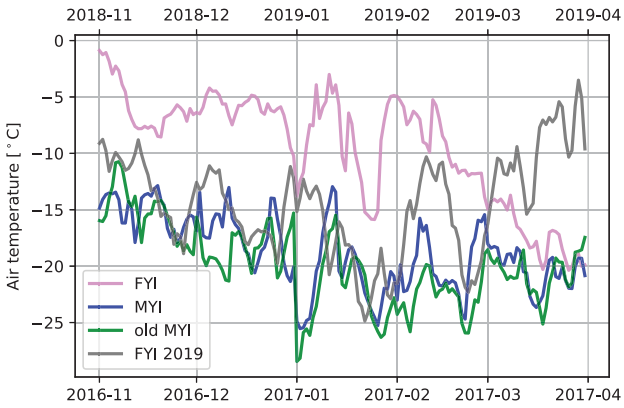

Fig. 2. Maximum air temperatures from ERA-5 centered in the investigation areas: Winter 2016/2017 in green, pink, and blue (lower time axis) and winter 2018/2019 in grey (upper time axis). Generated using Copernicus Climate Change Service Information (2016/2017; 2018/2019) [20].

B. SAR Imagery

Eight Sentinel-1B SAR image pairs acquired on December 5, 2016, December 29, 2016, January 22, 2017, and February 15, 2017 and one Sentinel-1 A SAR image pair taken on March 6, 2017 are used in this study. Each pair is composed of one image taken in ascending and one in descending orbital direction with large spatial overlap. The Sentinel-1 B image pairs are taken on the same relative orbit for both orbital directions with a repeat cycle of 24 d. Four pairs (violet in Fig. 1) are used for studying

FYI and four pairs (blue on Fig. 1) are used for MYI. Old MYI is studied for one Sentinel-1 A image pair (green in Fig. 1). Sea ice that has survived at least one summer melt is considered as MYI throughout this study, whereas old MYI refers to sea ice older than three years. In March 2018, improved noise removal was introduced for Sentinel-1 [23]. Four Sentinel-1 A images taken on December 5, 2018, December 29, 2018, January 22, 2019, and February 15, 2019 are used to investigate the impact of the improved noise removal on incidence angle dependence. The operational observation mode of Sentinel-1 no longer provides ascending images for most of the Arctic since May 2017, and, therefore, no image pairs could be obtained for later winters. Details about past and current observation strategies can be viewed at the ESA Sentinel-1 mission website[1] and the most recent one is detailed in the High-Level Operations Plan [24].

The SAR image mode is extra wide swath (EW) ground range detected with medium resolution (GRDM). The swath width of one SAR scene is 400 km with a resolution of about 100 m in range and azimuth and a pixel size of 40 $\times$ 40 m. The equivalent number of looks for this product is about 10.7 [25]. The time difference between ascending and descending passes varies between 13:20 and 15:00 h for the different locations with ascending images taken between 00:07 and 2:40 UTC and descending between 15:01 and 16:01 UTC. At local time, UTC-08:00, this corresponds to images taken late afternoon and morning the following day, respectively.

All images are in dual polarization with horizontal transmit and receive (co-polarization, HH) and horizontal transmit and vertical receive (cross-polarization, HV). Data from the season 2016/2017 is processed to GRD with Instrument Processing Facility (IPF) version 2.72 and data from 2018/2019 with IPF version 2.91. The data is preprocessed with the Sentinel Application Platform using the following steps: Precise orbit $\rightarrow$ noise removal $\rightarrow$ calibration to σ^0 $\rightarrow$ dB conversion $\rightarrow$ terrain correction with projection to UTM using ASTER 1 s GDEM. Pixel size is retained at 40 m.

The cross-polarization channel of Sentinel-1 is highly affected by thermal noise at areas of low backscatter intensities, typical of open ocean and smooth first-year ice [23]. Fig. 3 shows the mean annotated range noise profiles (lines) versus incidence angle for the used images. Below noise level values are possible because of the statistical and additive nature of the noise and the subtraction of the mean noise floor. The increased noise level of the first subswath is clearly visible for smaller incidence angles up to about 29°. Furthermore, large variations of the noise are observable at interswath boundaries. The annotated noise profile is not able to account completely for the additive noise. Even after noise correction, backscatter variations induced by residual noise remain at areas of low backscatter, especially between the first and second subswaths and at interswath boundaries; see Fig. 4. Noise removal has been improved for IPF versions starting from 2.9, corresponding to March 13, 2018. Most affected has been the scalloping noise in azimuth direction that

[1](https://sentinel.esa.int/web/sentinel/missions/sentinel-1/observation-scenario)

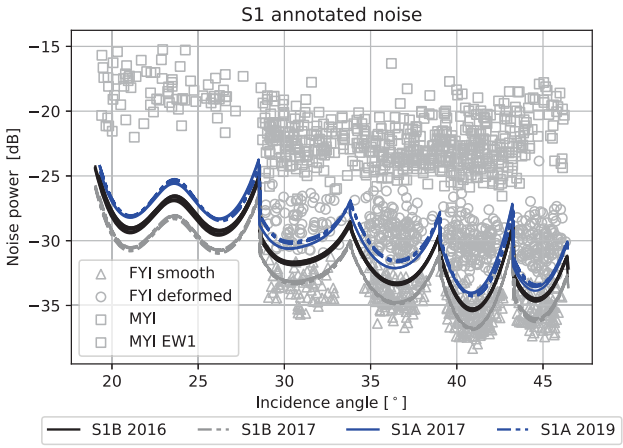

Fig. 3. Incidence angle dependence of the mean annotated Sentinel-1 HV range noise profiles (lines). Triangles, circles, and squares mark the HV backscatter intensities of smooth first-year, deformed first-year, and multiyear sea ice, respectively.

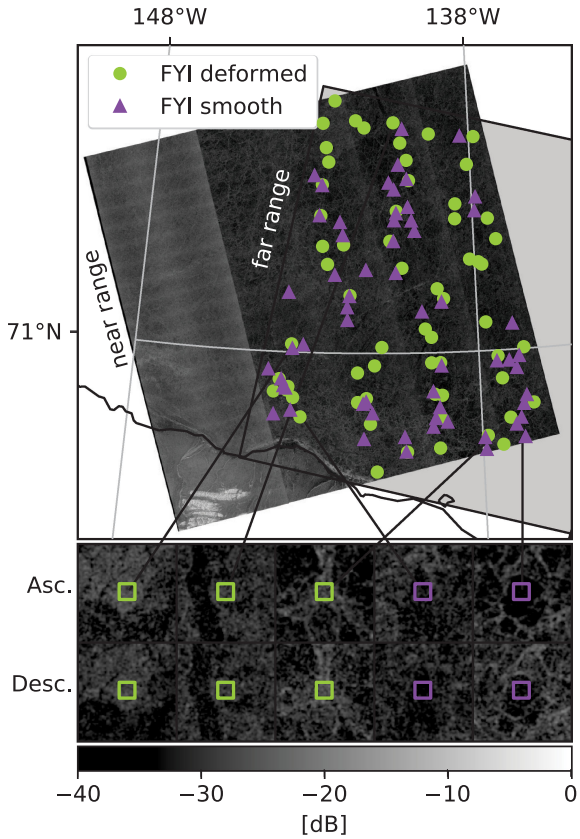

Fig. 4. Exemplary deformed (green) and smooth (purple) first-year sea ice samples at cross-polarization for the ascending image on January 22, 2017. Outlines of the descending image are shown as a grey box. Upper and lower rows of image zooms show selected samples for the ascending and descending pass. Contains Copernicus Sentinel-1 data 2017.

is significantly reduced for all subswaths by including noise profiles not only in range but also in azimuth [23]. The large difference between EW1 and EW2 could not entirely be resolved for the images used in this study [26] and the range noise

levels do not significantly change compared to the images from 2016/2017 (see Fig. 3).

III. Methodology

A. Sample Selection

In this article, three broad sea ice classes were analyzed for their backscatter intensity incidence angle dependence: Smooth FYI, rough/deformed FYI, and MYI. These classes were chosen to approximately span the range of expected angular dependencies, from high for smooth FYI to low for old MYI. Furthermore, with incidence angle normalization in mind, more classes would require extensive *a priori* knowledge of ice types, while the chosen classes can be roughly identified by backscatter intensity, texture, and contextual information.

Samples of the different classes were manually selected and matched for each image pair based on backscatter intensities, image texture, contextual information, and auxiliary ice charts, mainly from the Canadian Ice Service and also from the Russian Arctic and Antarctic Research Institute. Smooth FYI is characterized by a very low backscatter and smooth texture. Rough/deformed FYI shows an increased backscatter intensity and can have a smooth texture, e.g., brash ice or young ice, or shows texture due to, e.g., ridging. MYI has higher backscatter intensities compared to FYI. Volume scattering from air bubbles increases backscatter from old sea ice while surface scattering is dominant for younger sea ice [17]. Furthermore, MYI texture is usually rougher and more pronounced. Older MYI is characterized by generally increased backscatter values [27], [28]. In this study, older MYI refers to predominately more than three years of age while MYI mostly comprises second-year sea ice. The gradual change and subtle differences in backscatter intensities make it difficult to unambiguously identify sea ice age from backscatter characteristics and auxiliary information. Examples of selected FYI and MYI samples are shown in Figs. 4 and 5 for the ascending images of January 22, 2017.

The influence of radar speckle is reduced by calculating the mean backscatter intensity of a 17 $\times$ 17 pixels (680 $\times$ 680 m) window, whereby the incidence angle has been selected at the centre of each window. The window size was chosen as giving the best representative average backscatter value (not shown). Too small window sizes are sensitive to small-scale variations in backscatter intensities, while too large windows would cover different ice types.

The cross-polarization channel of Sentinel-1 contains residual noise contamination after thermal noise correction, as can be seen in Fig. 4. We therefore decided to exclude the first subswath (EW1) as well as subswath boundaries from our analysis of first-year ice samples. For multiyear ice, the impact of the residual noise is lower due to higher backscatter intensities. Hence, less care about subswath boundaries needed to be taken, but we nevertheless additionally investigated the effect of including the EW1 in our slope determination. The rightmost sample zoom in Fig. 5 shows the effect of EW1 especially for low backscatter areas, where the lower sample is located at EW1 of the descending image.

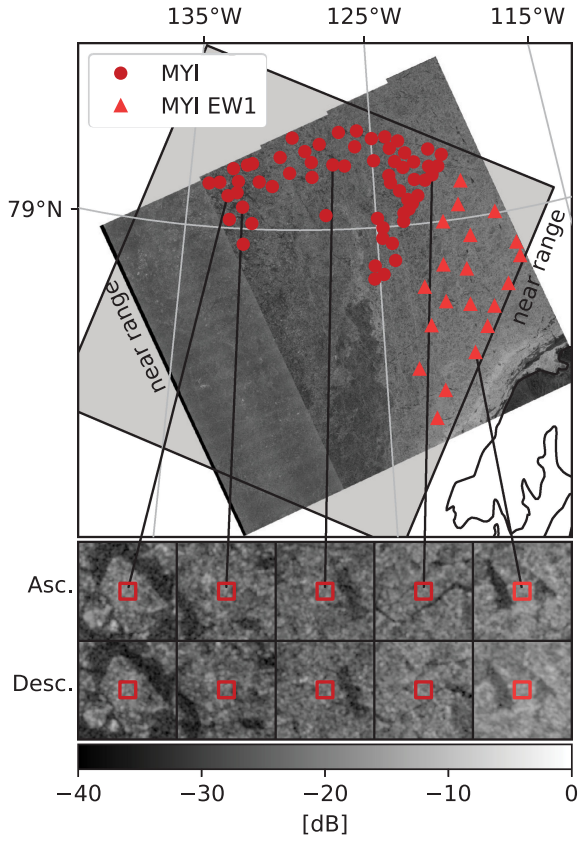

Fig. 5. Exemplary multiyear sea ice samples at cross-polarization for the ascending image on January 22, 2017. Outlines of the descending image are shown as a grey box. Upper and lower rows of image zooms show selected samples for the ascending and descending pass. Contains Copernicus Sentinel-1 data 2017.

FYI was studied for four image pairs outlined in violet in Fig. 1. Sixty samples for smooth and rough/deformed FYI, respectively, have been collected for each image pair, totaling to 240 samples per first-year ice type. MYI was studied for four image pairs outlined in blue and one image pair outlined in green in Fig. 1. Sixty samples have been collected for each blue image pair without EW1 and 20 samples per pair within EW1, totaling to 320 samples. For the single pair (green in Fig. 1), 100 samples without EW1 and 40 samples within EW1 have been collected. In addition, 100 samples have been selected for smooth and rough/deformed FYI in the images from 2018/2019.

B. Slope Determination

In this study, we adopted the method for slope determination presented in [14]. This method is based on the difference in incidence angle and backscatter intensity between two samples taken at different instances in time but representing the same patch of sea ice. This approach reduces the influence of natural variability in the backscattered signal within one ice class due to spatial changes in the physical and electrical properties of sea ice [6]. Therefore, fewer samples are needed for a robust estimate of incidence angle dependence. On the other hand, this method is sensitive to changes of backscatter intensities between the two acquisitions of a pair, i.e., by deformation through ice motion

TABLE I
SINGLE DAY SLOPE ESTIMATES

	Incidence Angle Slope [dB/1°]				
	20161205	20161229	20170122	20170215	all samples
FYI smooth HH	-0.23	-0.25	-0.23	-0.25	-0.24
FYI smooth HV	-0.14	-0.16	-0.17	-0.18	-0.16
FYI rough HH	-0.20	-0.22	-0.19	-0.200	-0.20
FYI rough HV	-0.12	-0.11	-0.11	-0.11	-0.11
MYI w/o EW1 HH	-0.14	-0.16	-0.15	-0.16	-0.15
MYI w/o EW1 HV	-0.07	-0.08	-0.08	-0.07	-0.07
MYI with EW1 HH	-0.15	-0.17	-0.16	-0.17	-0.16
MYI with EW1 HV	-0.09	-0.08	-0.09	-0.08	-0.09

as well as by features with view angle dependent backscatter values such as linear oriented features like ridges.

We use pairs of images taken the same day but at different orbital directions so that selected image samples are available at two different incidence angles. The difference in incidence angle is thus given by $\Delta\theta_{\text{inc}} = \theta_{\text{inc},a} - \theta_{\text{inc},d}$, where $\theta_{\text{inc},a}$ and $\theta_{\text{inc},d}$ are the incidence angles of the ascending and the descending image, respectively. The backscatter difference is calculated accordingly by $\Delta\sigma^0 = \sigma^0_a - \sigma^0_d$, where σ^0_a and σ^0_d are the backscatter intensities of the ascending and the descending image, respectively. The slope $\Delta\sigma^0/\Delta\theta_{\text{inc}}$ is obtained through linear regression of the scatter plot.

IV. RESULTS AND DISCUSSION

In this section, we first present and evaluate backscatter intensity σ^0 versus incidence angle slope estimates for different ice types. Thereafter, we analyze the benefits of incidence angle normalization.

A. Slope Estimation

Fig. 6 shows backscatter difference $\Delta\sigma^0$ versus incidence angle difference $\Delta\theta_{\text{inc}}$ scatter plots for the different ice types for co- and cross-polarization. Smooth FYI shows the highest incidence angle dependence with -0.24 and -0.16 dB/1° for co- and cross-polarization, respectively. Backscatter intensities for smooth FYI are however at or below the noise floor; see Fig. 3. Therefore, it is likely that the incidence angle distribution follows the noise floor rather than the real incidence angle dependence at cross-polarization. Rough/deformed FYI shows slightly lower slopes: -0.20 and -0.11 dB/1° for the two polarizations, respectively. MYI without the first subswath shows the lowest slopes in this study: -0.15 and -0.10 dB/1° at co-polarization and -0.07 and -0.04 dB/1° at cross-polarization for MYI and the case study of older MYI, respectively. The *R* squared values for all cases as well as the analysis of the residuals of the model (not shown here) indicate that a linear model is a valid choice for the incidence angle range of Sentinel-1.

Table I presents the individual incidence angle slope estimates for each of the four image pairs of FYI (purple in Fig. 1) and MYI (blue), along with the overall estimates we just discussed (Fig. 6(a)–(f)). Single date slopes agree well with the slopes retrieved from all dates combined. The evolution of sea ice throughout the study period does not seem to impact the retrieved slope. We therefore conclude that the presented slope estimates are representative for wintertime incidence angle dependence of backscatter intensity in the Beaufort Sea.

The decrease in slope from smooth FYI to old MYI as well as the lower slopes at cross-polarization are expected and can be explained by the dominant scattering mechanism for each ice type and polarization, respectively. Surface scattering, typical for FYI, is more affected by incidence angle changes than volume and multiple scattering characteristic for MYI [3], [29]. Backscatter of older sea ice is more dominated by volume scattering and hence the incidence angle dependence further decreases with the age of sea ice [30]. Furthermore, the cross-polarization backscatter signal originates from multiple scattering events and therefore shows a lower dependence on incidence angle compared to the co-polarization channel [31].

The co-polarization slopes for rough/deformed FYI and MYI compare well to a previous study of fast ice in the Canadian Archipelago from Radarsat-2 that estimated mean incidence angle dependence of -0.22 and -0.16 dB/1° from various roughness classes for FYI and MYI, respectively [8]. Furthermore, our slopes agree with estimates for FYI from Sentinel-1 in the Kara Sea that found slopes of -0.25 and -0.24 dB/1° for level and deformed FYI at co-polarization, respectively [6]. A recent study using direct incidence angle versus backscatter regression from Radarsat-2 in the Canadian Arctic reports slopes of -0.27 and -0.20 dB/1° for co-polarization FYI and MYI, respectively [7]. The cross-polarization slopes of the same study, -0.13 and -0.07 dB/1° for FYI and MYI, respectively, compare well with the estimates of this study. Cross-polarization slopes from Sentinel-1 in the Kara Sea, -0.24 and -0.16 dB/1° for smooth and deformed FYI, respectively, are slightly larger than that in our study [6]. One of the reasons can be the exclusion of the first subswath and avoidance of subswath boundaries in our study. The slope for deformed FYI in their study decreases if higher signal-to-noise ratios are required for the selected samples of deformed FYI. Conversely to a study including incidence angle dependence of different ice types during early winter in the Beaufort Sea [4], our slopes at cross-polarization are significant for all ice types and especially for FYI. One reason for this disagreement could be that in their study, the incidence angle dependence of FYI could have been buried in the noise floor of about -28 dB for the ScanSAR wide mode of Radarsat-2 [32]. The noise floor of Radarsat-2 is varying around about -28 dB but has no trend towards lower values at higher incidence angles.

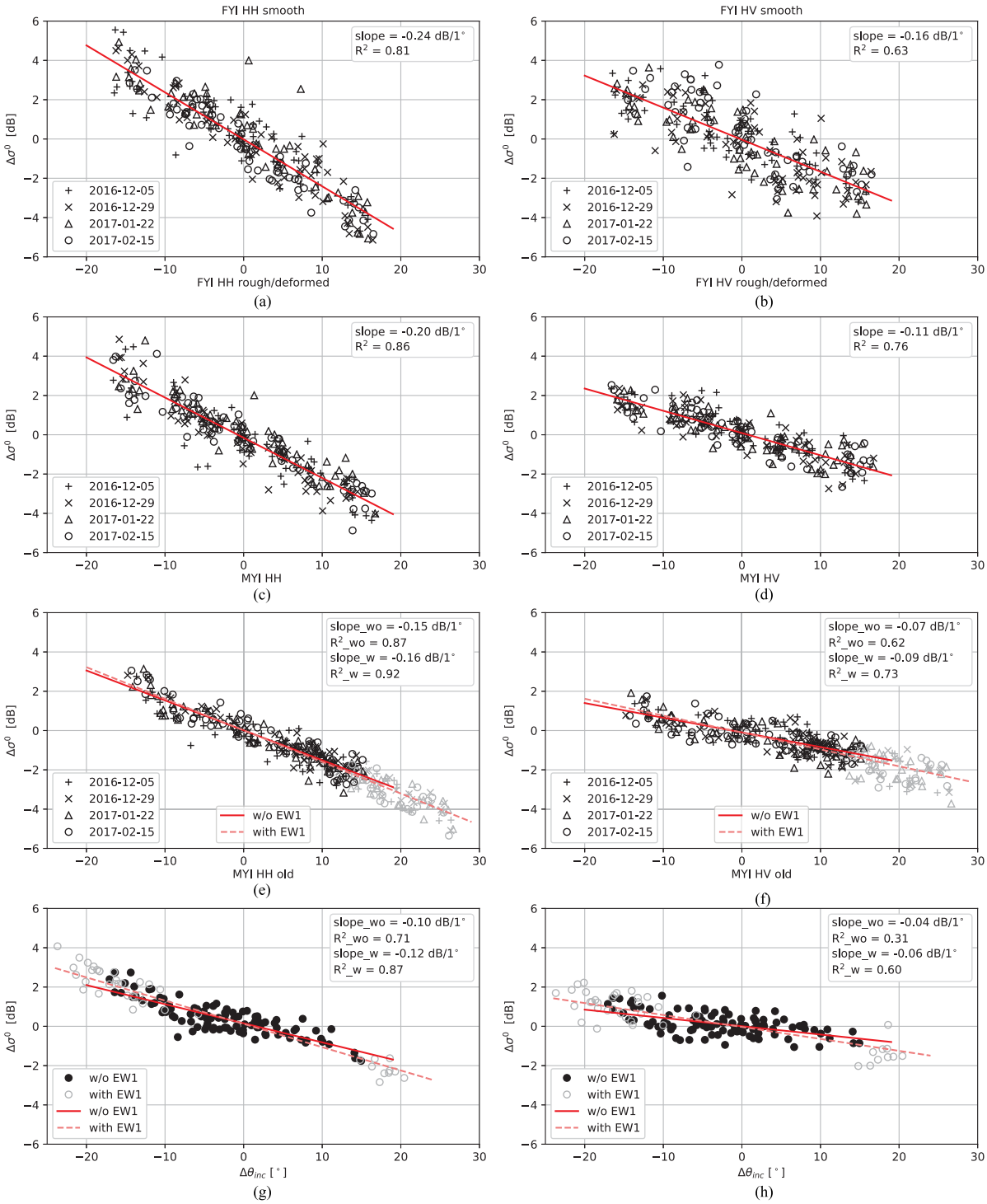

Fig. 6. Scatter plots of backscatter difference versus incidence angle difference for (a) smooth first-year ice HH, (b) smooth first-year ice HV, (c) rough first-year ice HH, (d) rough first-year ice HV, (e) multiyear ice HH, (f) multiyear ice HV, (g) old multiyear ice HH, and (h) old multiyear ice HV. Grey markings in plots (e)–(h) show samples from the first subswath. Red and dashed light red lines depict the slope estimate for each plot without and with first subswath, respectively.

Furthermore, only two images at the beginning of October have been used in that study. Table II summarizes the results presented in various studies for comparison with the results obtained in this study.

The generally good agreement with co-polarization slope estimates from other studies is a good proxy for the validity of the presented slope estimates at cross-polarization. Furthermore, they agree well with values obtained from Radarsat-2 imagery. The ability to detect cross-polarization incidence angle dependence for smooth FYI, however, requires a low enough noise floor, see Fig. 3, and, therefore, the results may not be transferable to sensors with different noise characteristics.

We also investigated the effect of including EW1 in the estimation of the incidence angle behavior of MYI. We limited

TABLE II
SUMMERY OF ESTIMATED SLOPES FROM RELEVANT STUDIES

	Sensor	Place	Method	Slope [dB/1°]
Mäkynen and Karvonen (2017) [6]	Sentinel-1	Kara Sea	difference	FYI smooth HH: -0.25 FYI smooth HV: -0.24 FYI deformed HH: -0.24 FYI deformed HV: -0.16
Mahmud et al. (2018) [8]	Radarsat-2	Beaufort Sea	direct (fast ice)	FYI HH: -0.22 MYI HH: -0.16
Komarov et al. (2019) [7]	Radarsat-2	Beaufort Sea	direct	FYI HH: -0.27 FYI HV: -0.13 MYI HH: -0.20 MYI HV: -0.07
This Study	Sentinel-1	Beaufort Sea	difference	FYI smooth HH: -0.24 FYI smooth HV: -0.16 FYI deformed HH: -0.20 FYI deformed HV: -0.11 MYI HH: -0.15 MYI HV: -0.07

this study to MYI because FYI samples are at or well below the noise floor, while MYI samples are above the noise floor of EW1; see Fig. 3. Furthermore, it is known that noise power scaling at EW1 over sea ice is insufficient to account for the noise completely [16] and the impact of the residual noise will be lower for higher backscatter intensities. This residual additive noise is expected to increase the slope of the incidence angle dependence. Inclusion of EW1, as shown in Fig. 6(e)–(h), increases the slopes slightly by −0.01 and −0.02 dB/1° for MYI and −0.02 dB/1° for old MYI at co- and cross-polarization, respectively. A slope of −0.01 dB/1° equates to a change of 0.27 dB over a range of incidence angles from 19° to 46°, and, therefore, the normalization result is only slightly impacted by the inclusion of EW1.

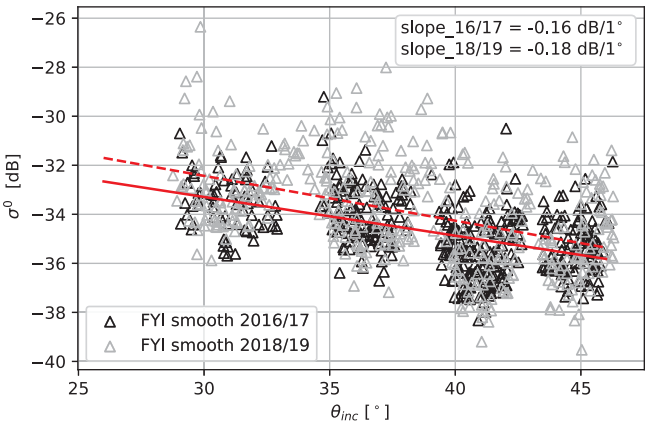

Fig. 7. Cross-polarization backscatter intensities versus incidence angle for smooth first-year sea ice in 2016/2017 (black triangles) and in 2018/2019 (grey triangles).

B. Impact of Improved Noise Removal

The improved noise removal of Sentinel-1 since March 2018 poses the question of how far the obtained results can be transferred to this new imagery. As explained in Section II-B, no analysis of difference in incidence angle and backscatter intensity can be conducted for these images. Therefore, we instead compare slope estimates for smooth and rough/deformed FYI at cross-polarization inferred directly from backscatter intensity versus incidence angle. As indicated in Fig. 3, backscatter intensities for MYI are, in general, significantly higher than the noise floor and are therefore less affected by the noise removal. In addition, MYI slopes are affected by natural changes in backscatter characteristics due to differences in age. For these reasons, effects of the improved noise removal on MYI slopes have not been analyzed.

Figs. 7 and 8 show backscatter intensity versus incidence angle for smooth and rough/deformed FYI, respectively. The larger spread of data points for 2018/2019 can partly be explained by different ice conditions between the two seasons resulting in higher backscatter values of deformed ice. Especially in December 2018, the ice was less consolidated with more leads. The variation is not so pronounced for the smooth ice case where samples clearly follow the noise floor pattern. Estimated slopes for the 2018/2019 season are −0.18 and −0.15 dB/1° for smooth and rough/deformed FYI, respectively. These slopes are slightly larger than those from 2016/2017 with −0.16 and −0.13 dB/1° and the estimates from difference in incidence angle and backscatter intensity. Differences between the two methods can originate in the sensitivity of the direct method to variability of backscatter intensities for similar incidence angles as well as to variations over the large swath width. It is a challenging task to collect samples spanning a similar range of backscatter intensities per incidence angle interval. Deviations at the extreme ends can have a large impact on the result. The difference method reduces this effect by comparing samples representing the same patch of ice.

Comparison between the years shows that there might be slight differences due to different overall ice situations, but the

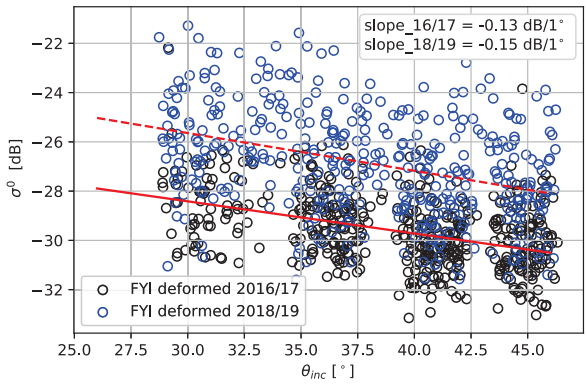

Fig. 8. Cross-polarization backscatter intensities versus incidence angle for rough/deformed first-year sea ice in 2016/2017 (black circles) and in 2018/2019 (blue circles).

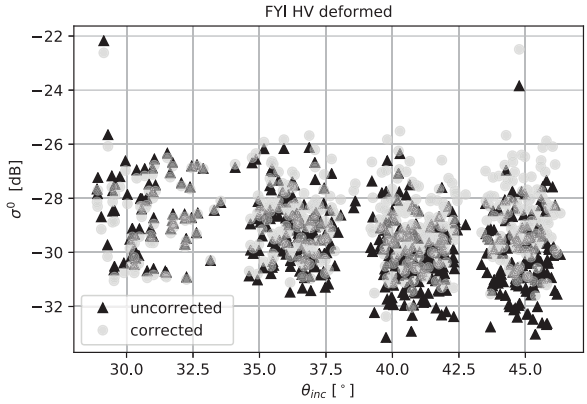

Fig. 9. Backscatter intensities versus incidence angle before (black triangles) and after (pale circles) incidence angle normalization to 33° for rough/deformed first-year sea ice.

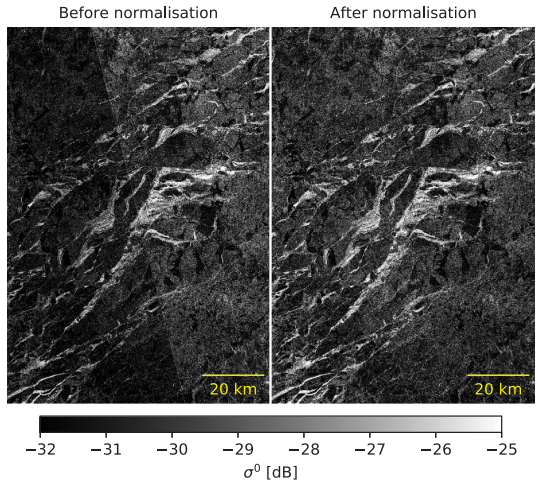

Fig. 10. Backscatter intensities (HV) before (left) and after (right) incidence angle normalization for first-year sea ice for an image pair acquired on December 5, 2016. Maximum incidence angle difference at the transition is about 13°.

general trends are very similar. The results are therefore also transferable to other parts of the Arctic because it is more the conditions under which the ice is formed than the region that determines the scattering conditions [17].

C. Incidence Angle Normalization

One way to account for incidence angle dependence is the normalization to a reference incidence angle to homogenize the backscatter intensities over the image width. We choose 33° as a reference, as this angle represents approximately the center of the image swath and ensures equal correction at near and far range. Incidence angle normalization at co-polarization has been widely used, and we, therefore, focus here on the evaluation of the cross-polarization case.

For rough/deformed FYI, the incidence angle slope of −0.11 dB/1° for cross-polarization equates to a change of backscatter intensity of about 3 dB over the incidence angle range (19°–46°). Fig. 9 shows the backscatter intensities versus incidence angle before (black triangles) and after (pale circles) normalization to the reference angle for rough deformed FYI. The ice cover in the study area can be considered homogeneous, and, therefore, no difference between ascending and descending samples is made. Due to the exclusion of EW1, only angles between 28° and 46° are shown in the figure. It can be seen that, as expected, the normalization levels out the trend of decreasing backscatter intensities with incidence angle.

The effect of incidence angle normalization is further underlined by comparing mosaics from the image pairs with large incidence angle difference before and after correction. The first subswath has been removed from the images to better demonstrate this effect. Fig. 10 shows a mosaic example from December 5, 2016 of FYI before and after normalization, where the ascending and descending images have simply been overlaid. Sea ice drift has not been taken into account, which can be noticed if the border between images is analyzed in more detail. Before normalization, the transition from one image to the other is clearly visible at the center of the left image in Fig. 10, while it disappears after normalization (right image in Fig. 10). Incidence angle normalization therefore can facilitate image interpretation not only of mosaics but also of SAR images that span a wide incidence angle range.

The MYI in this area is more difficult to assess because the age of the MYI is not homogeneously distributed in our image pairs. Fig. 11 shows the NSIDC sea ice age product [33] for February 12, 2017 to February 18, 2017 and the outline of the SAR images used for our MYI studies. Old MYI, which has a higher backscatter, is found in the far range for the ascending case but near range in descending. Plotting backscatter versus incidence angle dependence therefore needs to be done separately for the ascending and descending case because the highest backscatter is expected at far and near range for the two orbital directions, respectively. As backscatter intensity and texture are very similar, we were not able to distinguish different ages unambiguously and therefore used one single class. The incidence angle slope of −0.07 dB/1° for MYI at cross-polarization equates to a

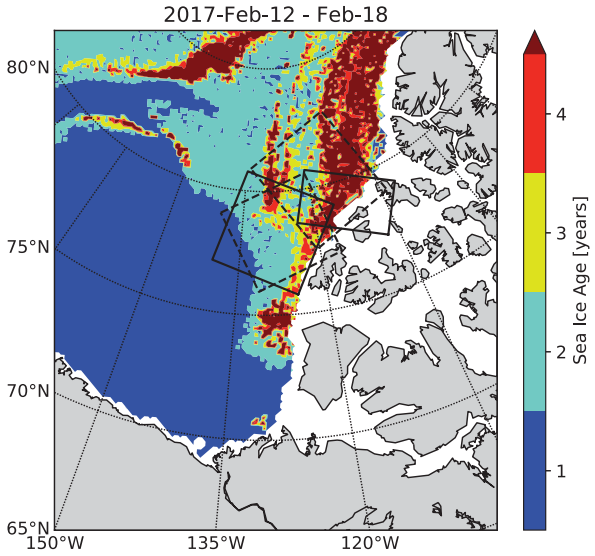

Fig. 11. NSIDC sea ice age distribution within the study area for the week February 12–18, 2017. Dashed and solid lines outline ascending and descending images, respectively [33].

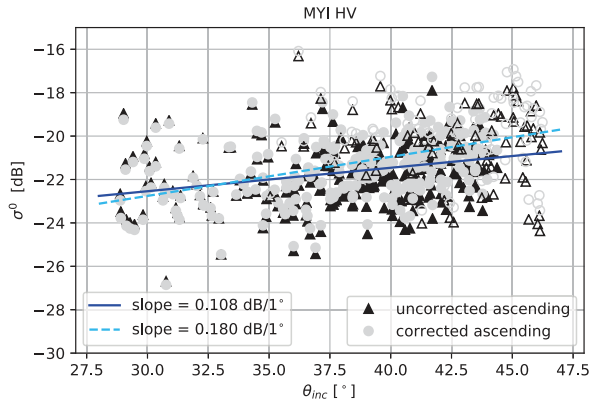

Fig. 12. Multiyear sea ice backscatter intensities versus incidence angle before (black triangles) and after (pale circles) incidence angle normalization to 33° for the ascending image samples. Blue and dashed light blue lines indicate the slope of the samples before and after incidence angle correction. Empty symbols mark samples located in EW1 of the descending image.

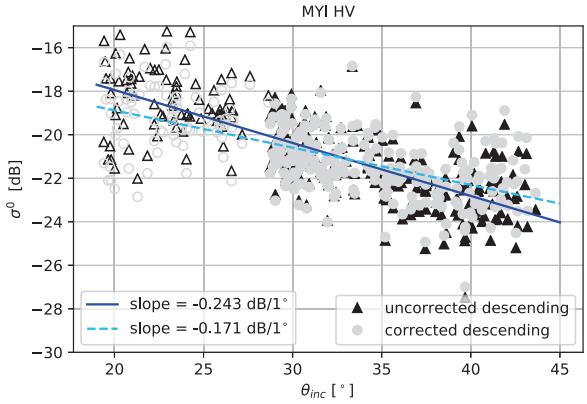

Fig. 13. Same as for Fig. 12 but for the descending image samples.

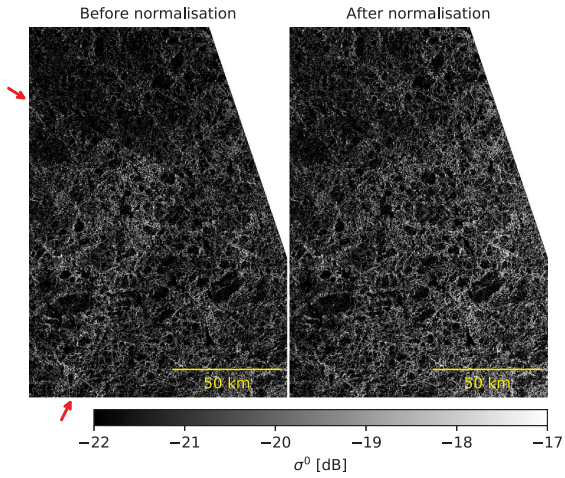

Fig. 14. Backscatter intensities (HV) before (left) and after (right) incidence angle normalization for multiyear sea ice for an image pair acquired on December 29, 2016. Maximum incidence angle difference at the transition is about 15.6°. Red arrows indicate boundaries of overlaid image.

difference in backscatter at near and far range of approximately 2 dB.

Figs. 12 and 13 show the incidence angle dependence of MYI samples from the ascending and descending images, respectively. For the ascending images, one observes an increasing trend of backscatter intensity with incidence angle and for the descending images, a decreasing trend is observed. This is due to the different look directions in perspective to the trend of sea ice age as shown in Fig. 11. Therefore, the incidence angle dependence is masked by the physical properties of the sea ice, i.e., increasing sea ice backscatter with age. As we take the difference of two samples from ascending and descending images, this natural variation is canceled out and slope determination is only slightly affected by a decreasing incidence angle dependence with sea ice age. This demonstrates that for slope determination from a single image, a homogeneous image is needed, which cannot always be guaranteed for a wide swath imagery. After incidence angle correction, the residual slopes of natural variability are more similar in absolute value than before correction. Care should be taken in directly comparing these slopes as the look direction and direction of sea ice age changes are slightly different for the ascending and descending cases.

Fig. 14 demonstrates the effect of incidence angle normalization for MYI with an example from December 29, 2016. Before normalization, the corner of the overlaid image is visible at the center of the image but nearly vanishes after incidence angle normalization. Due to the smaller angular dependence of MYI, the difference is not as pronounced as for the FYI case shown in Fig. 10. This example nevertheless illustrates that there is a benefit of incidence angle correction for MYI, even though this plays a role mostly for larger incidence angle differences.

V. Conclusion

In this article, we present an analysis of co- (HH) and cross-polarization (HV) incidence angle dependencies for different ice types from smooth FYI to old MYI from Sentinel-1 imagery. Although incidence angle dependence is smaller at cross-polarization compared to co-polarization, the estimated

slopes show a significant impact on wide swath SAR images. Two representative examples of overlays of ascending and descending images for FYI and MYI demonstrate the benefit of incidence angle dependence correction for visual, and therefore most likely also automatic, image interpretation. Our analysis also shows that the angular dependence decreases with the age of the sea ice, as volume and multiple scattering play a larger role for backscatter intensities [17]. With the Arctic sea ice getting younger and thinner [34], the benefit of incidence angle normalization will increase in the future.

Detection of incidence angle dependence for FYI at cross-polarization requires a high-enough signal-to-noise ratio, and, therefore, the results are not without caution transferable to other sensors, where the angular dependence of backscatter intensities could be buried in noise. Incidence angle normalization will not overcome the limitations induced by noise floor variability and incomplete noise removal of Sentinel-1 cross-polarization SAR images and artifacts remain in the imagery. The introduction of the new noise removal scheme with Sentinel-1 IPF 2.9, however, significantly reduces the noise artifacts, but problems with the first subswath remain [26]. The scientific community is constantly working on improving noise removal for better usability of the cross-polarization channel also for older IPF versions [16], [35], [36].

Application of incidence angle normalization is straightforward for SAR scenes with homogeneous ice type distribution, where the appropriate slope can be chosen to correct the entire image. For scenes with mixed ice types, especially FYI and MYI, incidence angle normalization becomes more difficult especially due to the relatively large differences between the ice types. Single slope correction with mean slope of the dominant ice types or with the slope of one preferred ice type are two possibilities. A rough classification by backscatter intensity before incidence angle normalization can be an alternative. It has been shown that incidence angle normalization with the mean incidence angle dependence does not necessarily improve the classification result [7] and the normalization strategy for mixed ice scenes therefore has to be chosen with care and according to the application.

The choice of relatively broad ice classes and the general agreement with FYI estimates in the Kara Sea indicates that the presented estimates are also valid at other regions of the Arctic. Interpretation of Sentinel-1 SAR mosaics of the Arctic, e.g., provided by the Technical University of Denmark via www.seaice.dk, and results from scatterometer measurements [28] show similar backscatter patterns in different parts of the Arctic for general ice types. Deviations mostly occur in marginal ice zones, e.g., the transition from open ocean into the pack ice. This is strengthened by the comparisons between direct slope estimates of the two winter seasons 2016/2017 and 2018/2019. Differences in the general ice situation did not greatly affect the obtained slopes. Incidence angle normalization is widely used for co-polarization SAR images to homogenize the radar backscatter of wide swath images but should also be considered for cross-polarization Sentinel-1 imagery.

Acknowledgment

The authors would like to thank the two anonymous reviewers whose comments greatly improved the quality of this article.

References

[1] W. Dierking, "Mapping of different sea ice regimes using images from Sentinel-1 and ALOS synthetic aperture radar," *IEEE Trans. Geosci. Remote Sens.*, vol. 48, no. 3, pp. 1045–1058, Mar. 2010.

[2] B. Scheuchl, D. Flett, R. Caves, and I. Cumming, "Potential of Radarsat-2 data for operational sea ice monitoring," *Can. J. Remote Sens.*, vol. 30, no. 3, pp. 448–461, 2004.

[3] S. Nghiem and C. Bertoia, "Study of multi-polarization C-band backscatter signatures for Arctic sea ice mapping with future satellite SAR," *Can. J. Remote Sens.*, vol. 27, no. 5, pp. 387–402, Oct. 2001.

[4] H. Liu, H. Guo, and L. Zhang, "SVM-based sea ice classification using textural features and concentration from RADARSAT-2 dual-pol ScanSAR data," *IEEE J. Sel. Topics Appl. Earth Observ. Remote Sens.*, vol. 8, no. 4, pp. 1601–1613, Apr. 2015.

[5] J. P. Gill, J. J. Yackel, T. Geldsetzer, and M. C. Fuller, "Sensitivity of C-band synthetic aperture radar polarimetric parameters to snow thickness over landfast smooth first-year sea ice," *Remote Sens. Environ.*, vol. 166, pp. 34–49, Sep. 2015.

[6] M. Mäkynen and J. Karvonen, "Incidence angle dependence of first-year sea ice backscattering coefficient in Sentinel-1 SAR imagery over the Kara Sea," *IEEE Trans. Geosci. Remote Sens.*, vol. 55, no. 11, pp. 6170–6181, Nov. 2017.

[7] A. S. Komarov and M. Buehner, "Detection of first-year and multi-year sea ice from dual-polarization SAR images under cold conditions," *IEEE Trans. Geosci. Remote Sens.*, vol. 57, no. 11, pp. 9109–9123, Nov. 2019.

[8] M. S. Mahmud, T. Geldsetzer, S. E. L. Howell, J. J. Yackel, V. Nandan, and R. K. Scharien, "Incidence angle dependence of HH-polarized C- and L-band wintertime backscatter over Arctic sea ice," *IEEE Trans. Geosci. Remote Sens.*, vol. 56, no. 11, pp. 6686–6698, Nov. 2018.

[9] N. Y. Zakhvatkina, V. Y. Alexandrov, O. M. Johannessen, S. Sandven, and I. Y. Frolov, "Classification of sea ice types in ENVISAT synthetic aperture radar images," *IEEE Trans. Geosci. Remote Sens.*, vol. 51, no. 5, pp. 2587–2600, May 2013.

[10] W. Lang, P. Zhang, J. Wu, Y. Shen, and X. Yang, "Incidence angle correction of SAR sea ice data based on locally linear mapping," *IEEE Trans. Geosci. Remote Sens.*, vol. 54, no. 6, pp. 3188–3199, Jun. 2016.

[11] N. Zakhvatkina, A. Korosov, S. Muckenhuber, S. Sandven, and M. Babiker, "Operational algorithm for ice–water classification on dual-polarized RADARSAT-2 images," *Cryosphere*, vol. 11, no. 1, pp. 33–46, 2017.

[12] D. Murashkin, G. Spreen, M. Huntemann, and W. Dierking, "Method for detection of leads from Sentinel-1 SAR images," *Ann. Glaciol.*, vol. 59, no. 76pt2, pp. 124–136, Mar. 2018.

[13] R. Moore, K. Soofi, and S. Purduski, "A rader clutter model: Average scattering coefficients of land, snow, and ice," *IEEE Trans. Aerosp. Electron. Syst.*, vol. AES-16, no. 6, pp. 783–799, Nov. 1980.

[14] M. P. Mäkynen, A. T. Manninen, M. H. Similä, J. A. Karvonen, and M. T. Hallikainen, "Incidence angle dependence of the statistical properties of C-band HH-polarization backscattering signatures of the Baltic sea ice," *IEEE Trans. Geosci. Remote Sens.*, vol. 40, no. 12, pp. 2593–2605, Dec. 2002.

[15] R. Torres *et al.*, "GMES sentinel-1 mission," *Remote Sens. Environ.*, vol. 120, pp. 9–24, May 2012.

[16] J.-W. Park, A. A. Korosov, M. Babiker, S. Sandven, and J.-S. Won, "Efficient thermal noise removal for Sentinel-1 TOPSAR cross-polarization channel," *IEEE Trans. Geosci. Remote Sens.*, vol. 56, no. 3, pp. 1555–1565, Mar. 2018.

[17] R. G. Onstott, "SAR and scatterometer signatures of sea ice," in *Microwave Remote Sensing of Sea Ice*, F. D. Carsey, Ed. Washington, DC, USA: American Geophysical Union, 1992, ch. 5, pp. 73–102.

[18] R. J. Galley, E. Key, D. G. Barber, B. J. Hwang, and J. K. Ehn, "Spatial and temporal variability of sea ice in the southern Beaufort Sea and Amundsen Gulf: 1980–2004," *J. Geophysical Res.*, vol. 113, no. C5, May 2008.

[19] R. J. Galley *et al.*, "Replacement of multiyear sea ice and changes in the open water season duration in the beaufort sea since 2004," *J. Geophysical Res., Oceans*, vol. 121, no. 3, pp. 1806–1823, Mar. 2016.

[20] Copernicus Climate Change Service (C3S), "ERA5: Fifth generation of ECMWF atmospheric reanalyses of the global climate," Copernicus Climate Change Service Climate Data Store (CDS), 2019-12
[21] G. W. K. Moore, A. Schweiger, J. Zhang, and M. Steele, "Collapse of the 2017 winter Beaufort High: A response to thinning sea ice?" *Geophys. Res. Lett.*, vol. 45, no. 6, pp. 2860–2869, Mar. 2018.
[22] S. E. Howell *et al.*, "Comparing L- and C-band synthetic aperture radar estimates of sea ice motion over different ice regimes," *Remote Sens. Environ.*, vol. 204, pp. 380–391, Jan. 2018.
[23] R. Piantanida, "Thermal denoising of products generated by the Sentinel-1 IPF," S-1 Mission Performance Centre, European Space Agency, Tech. Rep. MPC-0392, Nov. 2017.
[24] Copernicus Space Component Mission Management Team, "Sentinel High Level Observations Plan," COPE-S1OP-EOPG-PL-15-0020, Issue/Revision 3/0, Jul. 2019.
[25] "Sentinel-1 product definition," S1-RS-MDA-52-7440, Issue/Revision 2/7, European Space Agency, Mar. 2016.
[26] N. Miranda, "SNAP user forum, GRD-border-noise and thermal noise removal are not working anymore since March 13. 2018," Public Communication, 2018. [Online]. Available: https://forum.step.esa.int/t/grd-border-noise-and-thermal-noise-removal-are-not-working-anymore-since-march-13-2018/9332/9
[27] A. M. Swan and D. G. Long, "Multiyear arctic sea ice classification using quikscat," *IEEE Trans. Geosci. Remote Sens.*, vol. 50, no. 9, pp. 3317–3326, Sep. 2012.
[28] M. B. Rivas, I. Otosaka, A. Stoffelen, and A. Verhoef, "A scatterometer record of sea ice extents and backscatter: 1992–2016," *Cryosphere*, vol. 12, no. 9, pp. 2941–2953, Sep. 2018.
[29] A. K. Fung, *Microwave Scattering and Emission Models and Their Applications*. Norwood, MA, USA: Artech House Inc., 1994, ch. 9, pp. 373–418.
[30] A. Carlström and L. Ulander, "C-band backscatter signatures of old sea ice in the central Arctic during freeze-up," *IEEE Trans. Geosci. Remote Sens.*, vol. 31, no. 4, pp. 819–829, Jul. 1993.
[31] M. Shokr and N. Sinha, *Sea Ice: Physics and Remote Sensing*. Hoboken, NJ, USA: John Wiley & Sons, 2015, ch. 7, pp. 271–335.
[32] "RADARSAT-2 product description," RN-SP-52-1238, Issue/Revision 1/14, Maxar Technologies Ltd., Richmond, B.C., Canada, Sep. 2018.
[33] M. Tschudi, W. N. Meier, J. S. Stewart, C. Fowler, and J. Maslanik, 2019, "EASE-Grid Sea Ice Age, Version 4," Boulder, Colorado USA, NASA National Snow and Ice Data Center Distributed Active Archive Center. doi: 10.5067/UTAV7490FEPB
[34] R. Kwok, "Arctic sea ice thickness, volume, and multiyear ice coverage: Losses and coupled variability (1958–2018)," *Environ. Res. Lett.*, vol. 13, no. 10, Oct. 2018, Art. no. 105005.
[35] J.-W. Park, J.-S. Won, A. A. Korosov, M. Babiker, and N. Miranda, "Textural noise correction for Sentinel-1 TOPSAR cross-polarization channel images," *IEEE Trans. Geosci. Remote Sens.*, vol. 57, no. 6, pp. 4040–4049, Jun. 2019.
[36] J. Karvonen, "Baltic sea ice concentration estimation using SENTINEL-1 SAR and AMSR2 microwave radiometer data," *IEEE Trans. Geosci. Remote Sens.*, vol. 55, no. 5, pp. 2871–2883, May 2017.

Wiebke Aldenhoff received the Diplom-Physiker degree from Clausthal University of Technology, Clausthal, Germany, in 2012. She is currently working toward the Ph.D. degree in radar remote sensing of sea ice at Chalmers University of Technology, Göteborg, Sweden.

Her main focus is on multifrequency synthetic aperture radar imagery and radar altimetry to retrieve sea ice information.

Leif E. B. Eriksson received a University Certificate in space technology from Umeå University, Umeå, Sweden, in 1993, the M.S. degree in electrical engineering from Chalmers University of Technology, Gothenburg, Sweden, in 1998, and the Ph.D. degree from Friedrich-Schiller University, Jena, Germany, in 2004.

From 1999 to 2000, he was employed with the Joint Research Centre of the European Commission, Space Application Institute, Ispra, Italy, where he was working with ERS data for forest and wetland mapping in Siberia. Between 2000 and 2004, he was with the Department of Geoinformatics, the Friedrich-Schiller University, Jena, Germany, where he was working with C-band and L-band SAR interferometry for forestry applications. In 2004, he joined the Radar Remote Sensing Group, Chalmers University of Technology, Gothenburg, Sweden, where, since 2012, he holds a position as Associate Professor in radar remote sensing with the Department of Space, Earth and Environment. His research interests include the use of SAR to retrieve information about ocean, sea ice, and forest.

Yufang Ye received the B.S. degree in physics and the M.S. degree in remote sensing from Beijing Normal University, Beijing, China, in 2008 and 2011, respectively, and the Ph.D. degree in environmental physics from the University of Bremen, Bremen, Germany, in 2016.

Between 2016 and 2017, she was with the group of "Remote Sensing of Polar Regions," Institute of Environmental Physics, University of Bremen, Bremen, Germany, working on sea ice monitoring with scatterometer and radiometer data. From 2017 to 2019, she was with the Radar and Optical Remote Sensing Division, Department of Space, Earth and Environment, Chalmers University of Technology, Gothenburg, Sweden, where she was working with SAR data for ocean and sea ice applications. Since 2020, she has been holding a position as Assistant Professor with School of Geospatial Engineering and Science, Sun Yat-Sen University, Guangzhou, China. Her research interests include microwave remote sensing of polar regions with focus on monitoring changes of sea ice (concentration, type, and dynamics) and understanding the mechanisms behind.

Céline Heuzé received the Engineering degree and the M.S. degree in hydrodynamics and ocean engineering from the Ecole Centrale de Nantes, Nantes, France, in 2011, and the Ph.D. degree in physical oceanography from the University of East Anglia, Norwich, U.K., in 2015.

From 2015 to 2018, she was with the Department of Marine Sciences, University of Gothenburg, Gothenburg, Sweden, as a VINNMER Marie Curie Research Fellow, working on the interaction between warm Atlantic Water and Greenland glaciers, using ship-based observations and global climate modeling. In parallel, she acted as a Consultant on ocean remote sensing for Chalmers University of Technology, inferring ocean surface currents from spaceborne infrared. Since 2018, she has been holding a position as Associate Senior Lecturer in climatology with the Department of Earth Sciences, University of Gothenburg. Her research interests include ocean–sea ice heat exchanges in the polar region, notably in under-observed regions or periods.